Materials Today Energy 19 (2021) 100560

Contents lists available at ScienceDirect

Materials Today Energy

journal homepage: www.journals.elsevier.com/materials-today-energy/

Mesoporous carbon aerogel with tunable porosity as the catalyst support for enhanced proton-exchange membrane fuel cell performance

K. Gu [a, c], E.J. Kim [a, c], S.K. Sharma [b], P.R. Sharma [b], S. Bliznakov [a], B.S. Hsiao [b], M.H. Rafailovich [a, *]

[a] Department of Materials Science and Chemical Engineering, Stony Brook University, Stony Brook, NY, 11794, United States
[b] Department of Chemistry, Stony Brook University, Stony Brook, NY, 11794, United States

ARTICLE INFO

Article history:
Received 8 July 2020
Received in revised form
4 October 2020
Accepted 7 October 2020
Available online 14 October 2020

Keywords:
Catalyst utilization
Durability
Mesoporosity
Uniform distribution
ECSA

ABSTRACT

Proton-exchange membrane fuel cells (PEMFCs) are considered to be one of the most promising clean technologies to mitigate climate change, air pollution, and energy crisis. Although PEMFCs have been intensively investigated over the past five decades, the relatively low current density, high cost, and poor durability remain as obstacles to full commercialization. In this study, we present the development and the application of a porosity-tunable carbon aerogel (CA) as an alternative to the carbon support in the PEMFC to overcome its technical barriers. CA demonstrates highly tunable mesopore volume and surface area. The N_2 isotherm with non-localized density functional theory analysis shows the optimized CA had extremely high mesopore volume, which was 4.26 times larger than the traditional carbon support (i.e., Vulcan XC-72R). Transmission electron microscopy shows a better catalyst (i.e., platinum nanoparticles) distribution on the CA support. This even distribution of platinum nanoparticles significantly enhances the catalyst utilization of the electrodes in our cyclic voltammetry analysis. It also contributes up to a 713% higher specific power density in our fuel cell testing. The standard accelerated stress tests exhibit that CA has excellent durability compared with the conventional carbon support. Thus, the mesoporous CA provides an efficient and durable alternative to existing carbon material as a catalyst support in PEMFCs.

1. Introduction

More than 1 billion gasoline cars worldwide emit 1.4 billion metric tons of greenhouse gases per year and are among the largest contributors to the growing global warming crisis, posing a challenging issue in sustainable development [1]. Furthermore, gasoline-based transportation accounts for 30% of $PM_{2.5}$ pollution and 2.38 million tons per year of airborne volatile organic compounds in the US. These pollutants not only bring environmental problems such as reduced visibility and decreased ecosystem biodiversity but also impose adverse health effects to the public [2,3]. Thus, it is a critical issue to find a sustainable alternative to reduce greenhouse gas emissions. In the past decades, many clean technologies, for example, wind and solar energy, have been intensively investigated in hopes of replacing gasoline to mitigate its environmental and public health stress [4,5]. Proton-exchange membrane fuel cells (PEMFCs) have attracted significant attention as a promising clean energy source owing to its zero greenhouse gas emission, high energy efficiency, and low operating temperature [6–8]. In the past decades, many PEMFC research efforts have been focused on catalyst development to increase its catalytic performance. However, the poor catalyst utilization in the catalyst layer and low durability still restrict further PEMFC performance improvements and thus limits its commercialization potential and availability in the consumer market [9–11].

The drawbacks of poor catalyst utilization and low durability are highly associated with the catalyst support in the PEMFC. The most commonly used and investigated catalyst supports in the PEMFC include carbon black (CB) [12–15], carbon nanotubes [16–20], and graphene [21–24]. CB, in particular, is a widely used catalyst support owing to its cheap cost of production and wide availability.

* Corresponding author.
E-mail address: miriam.rafailovich.sbu@gmail.com (M.H. Rafailovich).
[c] These authors contributed equally to this work.

https://doi.org/10.1016/j.mtener.2020.100560
2468-6069/

However, its high micropore volume, aggregated mechanical structure, and low conductivity all contribute to poor performance in the PEMFC by limiting the diffusion of reactants and products [25]. Other varieties of carbon support materials such as carbon nanotubes and graphene-based aerogels have stronger mechanical durability but are not suitable for commercialization owing to their high manufacturing costs and difficulty in catalyst impregnation [26,27].

Oxygen transport resistance at the catalyst surface has been identified as the primary contributor to poor catalyst utilization [28,29]. It is caused by poor catalyst distribution and constrictive pore structures in the catalyst support [28,30,31]. Poor catalyst distribution results in low electrochemical surface area (ECSA) and high oxygen transport resistance as it is inversely proportional to the catalyst surface area [28]. The ECSA is a routine descriptor of the active surface area that is electrochemically accessible in fuel cells. It is usually determined by cyclic voltammetry (CV) analysis. The procedure involves cycling the electrode of interest over a voltage range wherein charge transfer reactions are adsorption limited at the activation sites, that is, the electrode potential is such that the number of reactive surface sites can be obtained by recording the total charge required for monolayer adsorption/desorption. The ECSA of the Pt catalyst is calculated using the following equation:

$$ECSA = \frac{Q_{Pt}}{\Gamma^* L}$$

where Q_{Pt} is the charge density (C/cm^2) of the electrode from CV experimental data, Γ is the charge needed for reducing a monolayer of protons on Pt and equals to 210 μC/cm^2 for Pt, and L is the Pt mass loaded on a working electrode in the unit of g/cm^2. Therefore, improving fuel cell performance is contingent on maintaining a high ECSA per catalyst mass. In addition, poor fuel cell durability and performance can be attributed to both detachment of catalyst particles from the carbon support and catalyst coarsening due to particle coalescence, which is a result of catalyst particle reshaping on the catalyst support [32]. Both issues can be mitigated by improving the structural properties of the catalyst support, which are explored far less than catalyst materials [33].

Tuning the porosity of the catalyst support can directly change the ECSA and, thus, the oxygen transport resistance. Kumaraguru [34] suggested that mesopores play a significant role in reducing proton and oxygen transportation resistance. It was found that micropore volume was correlated with oxygen transport resistance, and macropore volume was correlated with proton transport resistance. Thus, the mesopore volume of the catalyst support plays a critical role in determining the reactant flow and general performance of the PEMFC. Xu and Zhao [35] found that the mesopore structure also improves the distribution of platinum nanoparticles in the pores and the overall surface. In this work, we aim to design, develop, and optimize the porosity of carbon aerogel (CA) to increase the overall performance of the catalyst support in the PEMFC by increasing the ECSA, promoting an even Pt nanoparticle distribution over the catalyst support surface, enhancing catalyst utilization, and raising durability of the electrode. The porosity of the CA can be tuned by changing the resorcinol/catalyst (R/C) ratio in the CA preparation process [36].

We first introduce a CA synthesis by solgel polymerization of resorcinol and formaldehyde and then describe the deposition of platinum nanoparticles onto the CA through the sodium borohydride reduction method [33,37]. The porosity and pore size distribution (PSD) of the developed materials are characterized by nonlocalized density functional theory (NLDFT). The platinum distribution and catalyst particle size are characterized by transmission electron microscopy (TEM). Then, CA is evaluated by comparing its performance to one of the most widely used CB materials, Vulcan XC-72R, which has good compromise between its adequate surface area and electric conductivity. Both CV testing and fuel cell testing were carried out. Accelerated stress tests (ASTs) following the DOE2020 protocol were also conducted to demonstrate its durability as the catalyst support.

2. Materials and methods

2.1. Materials

All chemicals were analytically pure and used as received without further purification. Chemicals for CA synthesis included resorcinol, sodium carbonate, formaldehyde solution (37% wt solution), and acetone (≥99.5% purity). All of them were obtained from Sigma-Aldrich (St. Louis, MO). Materials used for platinum impregnation on CA included chloroplatinic acid hexahydrate ($H_2PtCl_6 \bullet 6H_2O$) and sodium borohydride ($NaBH_4$) (99% purity), which were also obtained from Sigma-Aldrich (St. Louis, MO). Nafion® HP, Nafion® ionomer solution (15 wt%), Sigracet 29 BC carbon paper, and the CB Vulcan XC-72R from Cabot Corp. (Boston, MA) were used for electrode preparation and were from Fuel Cell Store (Austin, TX). H_2 (prepurified, 99.99%), O_2 (zero-grade, 99.8%), N_2 (zero-grade, 99.998%), and air (dry, 20–22% O_2) were purchased from Airgas Inc. (Radnor, PA).

2.2. CA synthesis

The CA was synthesized in order of solgel polymerization, solvent exchange, ambient drying, and carbonization. The process was sketched in Fig. 1. To produce CAs with R/C ratios of 100, 200, and 300, we prepared 1.54 g, 3.08 g, and 4.62 g of resorcinol (R), respectively. Each was separately prepared using 0.016 g of sodium carbonate (C) and dissolved in 50.4 mL of deionized water (DI water; W). The mixtures were magnetically stirred for 20 min at room temperature. A volume of 0.51 mL of 37% wt. formaldehyde (F) solution was added to the mixtures and stirred for an additional 5 min. The mixtures were heated in sealed containers at 50 °C for 24 h and then at 85 °C for another 48 h. The R-F gels were washed with excess amounts of acetone, solvent exchanging every 24 h. The gels were then dried in a vacuum oven at 100 °C. The organic gels were then carbonized in a Lindberg Blue M Tube Furnace. The R-F aerogels were loaded into three ceramic boats. Each boat was carbonized at a 10 °C/min temperature ramp rate to 800 °C, with a holding time of 2 h under N_2 atmosphere. After pyrolysis, the furnace was allowed to cool to 300 °C.

2.3. Catalyst impregnation of CA and CB

Fig. 1c shows the catalyst impregnation of CAs and CB. The CA and CB were each grounded using an agate mortar to obtain fine powders. One hundred milligrams of each carbon powder was individually dispersed into 80 mL of DI water. The mixtures were then stirred for 20 min and further sonicated for another 20 min. A volume of 2.6 mL of 0.1 M H_2PtCl_6 was added to the solutions drop by drop under continuous magnetic stirring. The mixtures were sonicated additionally for 20 min. A stoichiometric excess of 0.6 M $NaBH_4$ was dispersed dropwise as the reducing agent and sonicated for 1 h. The solutions were finally filtered using a Büchner funnel and washed 5 times with DI water. The desired Pt/CA and Pt/CB powders were obtained after heating at 80 °C overnight.

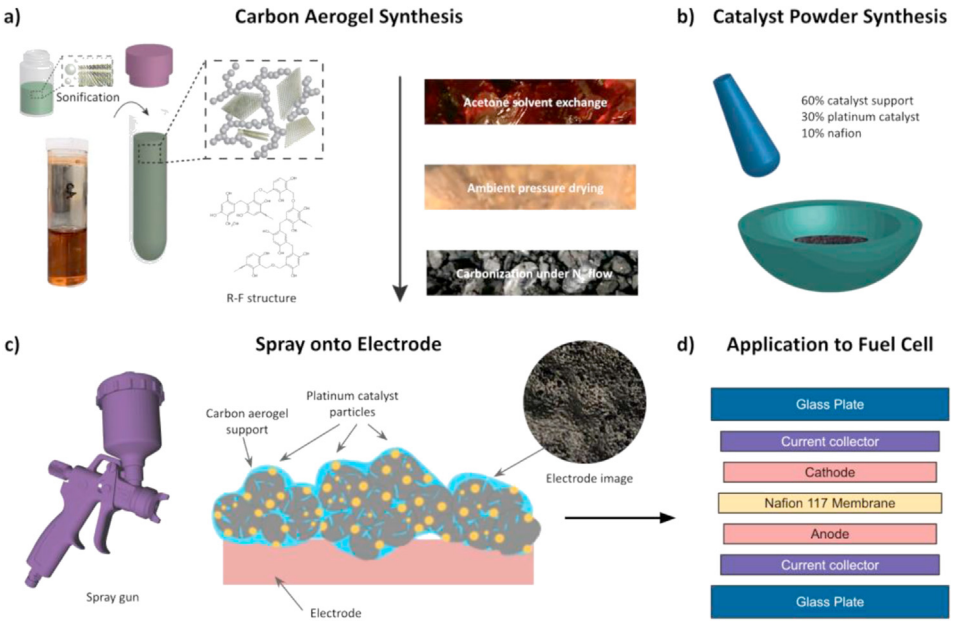

Fig. 1. (a) Synthesis of CA, (b) the Pt/catalyst (e.g., Pt/CA or Pt/CB) preparation, (c) application onto electrode, and (d) membrane electrode assembly (MEA) preparation. CA, carbon aerogel; CB, carbon black.

2.4. Membrane electrode assembly preparation

Fig. 1d demonstrates membrane electrode assembly (MEA) preparation. The homogenous catalyst inks were prepared by stirring a mixture of catalyst powder, Nafion ionomer, and 2-propanol at a mass ratio of 3:2:150. The ink was airbrushed onto the 5 cm^2 Sigracet 29 BC carbon paper. The papers were placed onto a hot plate to keep the surface temperature of the paper at 85 °C to evaporate the excess liquid. Electrodes with the desired Pt loading of 0.1 mg/cm^2 (30 wt%) were obtained for both the cathode and anode. The MEA was prepared by hot pressing the carbon papers with the 5 cm^2 Nafion 117 membrane under conditions of a pressure of 4 MPa at 130 °C for 1 min.

2.5. Characterization

Both Fourier transform infrared (FTIR) and Raman spectroscopy were used to collect the molecular fingerprint of CA and CB (see Figs. S1 and S2, respectively, in supplementary information). FTIR spectra between 500 and 4000 cm^{-1} were obtained on a Nicolet 6700 spectrometer. Raman spectra between 10 and 4000 cm^{-1} were obtained on a Renishaw InVia Raman spectrometer using incident laser light at a wavelength of 514.5 nm. Nitrogen adsorption and desorption measurements were carried out using a gas sorption analyzer (NOVAtouch LX^2, Boynton Beach, FL). NLDFT was used to model the pore distribution and surface areas. TEM images with 50× magnification were obtained on a JEM 1400Flash (JEOL, Peabody, MA). The TEM images were analyzed using ImageJ software to analyze the different catalyst particle sizes in the observed samples.

2.6. Evaluation of fuel cell performance and durability

The single-cell performance and durability were tested on a fuel cell test station from Fuel Cell Technologies, Inc. using the prepared MEAs. The polarization curves for the H_2/air fuel cell and the H_2/O_2 fuel cell were generated at both 60 °C and 80 °C under 100% relative humidity (RH) and 150 kPa_{abs} back pressure. After testing, the cathode was purged with N_2. CV was performed using the standard hydrogen electrode as the reference electrode as the anode and the different platinum on carbon electrodes as the cathode. The voltammetry was conducted at a scan rate of 20 mV/s with H_2 flowing on the anode and N_2 on the cathode to investigate cycling durability and observe the change in ECSA. To evaluate the durability of the MEAs, a standard AST was conducted using a potentiostat (Biologic P200) by square-wave cycle: steps between 0.6 V (3 s) and 0.95 V (3 s) with a rise time of 0.5 s and run polarization curve. Ten thousand AST cycles were performed under H_2/N_2 environment at 80 °C and 100% RH under atmospheric pressure with a fixed H_2 and N_2 flow of 200 sccm.

3. Results and discussion

3.1. Catalyst support characterization: nitrogen adsorption isotherms and porosity analysis

Fig. 2a shows the nitrogen adsorption-desorption isotherms of CB, CA-100, CA-200, and CA-300. All the materials exhibit Type IV isotherms with an H3 hysteresis loop as per the International Union of Pure and Applied Chemistry (IUPAC) classification [38]. Type IV isotherms are a characteristic of mesoporous materials because of the hysteresis loop from capillary condensations, which usually happen within mesopores [19]. The H3 hysteresis loop represents the characteristic slit-shaped pores and is commonly observed for carbonaceous materials [38]. Adsorption for this type IV material starts with micropore (<2 nm) volume filling, which is governed by the adsorption enthalpy that is strongly enhanced by the adsorption forces from the walls of the pore. This physical adsorption in micropores usually happens at very low gas particle pressure ($p/p_0 < 0.001$). In the medium and high partial pressure range, the monolayer and multilayer adsorption keep N_2 filling the external surface of the material and the mesopores (>2 nm) until the pore radius related to the capillary condensation at a given partial pressure is reached. At the capillary condensation stage, the mesopores are steeply filled. As the partial pressure approaches unity, all pores are filled with N_2, and theoretically, the isotherm reaches a

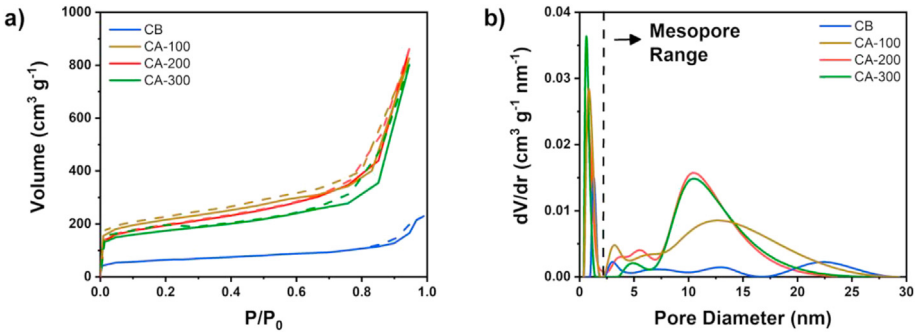

Fig. 2. (a) N_2 adsorption isotherms of CB, CA-100, CA-200, and CA-300 at 77 K, with a solid line for adsorption and dashed line for desorption, and (b) their respective pore size distributions. CB, carbon black.

plateau. In practice, the plateau or the saturation point is usually not observed because the macropores formed among the adjacent material particles continue uptaking N_2 [20].

The hysteresis loops are more pronounced and extended in a broader partial range in CAs, although all CAs and CB show hysteresis loop adsorption. These larger hysteresis loops spanning the wider particle pressure imply more mesopores and a larger mesopore volume (i.e., the larger hysteresis loops) and larger fraction of the mesopore porosity (i.e., the wider range of partial pressure of the hysteresis loop). Table 1 summarizes pore volume (V) data for micropores and mesopores (i.e., V_{micro} and V_{meso}, respectively), surface area (S) data for micropores and mesopores (i.e., S_{micro} and S_{meso}, respectively), average pore size (d_{avg}), total volume (V_{total}), and the total Brunauer-Emmett-Teller (BET) surface area (S_{BET}). It shows that mesopore volume of CAs is 3.0–4.2 times the volume of CB, and CA possesses a higher mesopore volume percentage in CAs. Among all three CAs, CA-200 has the largest V_{total} and V_{meso}, which are 1.314 and 1.143 cm^3/g, respectively, while V_{total} and V_{meso} of CB are 0.333 and 0.268 cm^3/g, respectively.

Fig. 2b shows the PSD of CAs and CB. All materials have micropore volume (pore diameter <2 nm), although the incremental volumes are varied. In the mesopore size range (2 nm < pore diameter < 50 nm), the PSD patterns of the CAs are clearly distinct from the PSD pattern of CB. CB possesses a flat and stretched PSD curve, and no single maximum pore size was observed, whereas all CAs share a similar PSD curve pattern, with the incremental volumes peaking at 12.5 nm, 10.5 nm, and 10.5 nm for CA-100, CA-200, and CA-300, respectively. It is noted that the d_{avg} could misrepresent the porosity of the material. For instance, the d_{avg} of CA is only 1.4 times the d_{avg} of CB, while the V_{total} and S_{BET} of CA-200 are 4.2 and 2.7 times the V_{total} and S_{BET} of CB, respectively. Thus, further analysis of pore parameters for micropores, mesopores, and macropores, separately, is essential for porosity investigation of CB and CA. Table 1 serves this purpose to present the parameters for all types of pores identified in all 4 materials in this study.

The micropores are believed to have a negative impact on the performance of the PEMFC because the Pt particle sizes are usually 2–4 nm. The catalyst is impossible to be deposited into micropores. Thus, only V_{meso} and S_{meso} are capable of depositing Pt nanoparticles. It is also believed that the edge sites of the micropores are highly reactive, and the agglomeration of Pt nanoparticles could be initiated at the necks of the micropores, which will be discussed later in this study [39]. Collectively, the micropores hinder the PEMFC performance. In addition, the mesopores promote ionomer loading to create the network for well-sufficient proton conduction and gaseous transportation for H_2 and O_2. A larger V_{meso} and S_{meso} and smaller V_{micro} and S_{micro} improve the PEMFC performance because of the larger amount of Pt deposition in pores and on the external surface, less Pt agglomeration, higher ionomer loading, and better gaseous transportation room. We thus chose CA-200 as our best CA representative for further investigation of its superior performance in the PEMFC against the standard catalyst support, CB.

3.2. Catalyst on CA-200 and CB characterization

The work in this section was conducted to characterize the most commonly used catalyst, Pt nanoparticles, in the PEMFC after the catalyst powders were deposited on a catalyst support, CA-200 and CB (see Fig. 1d). Fig. 3a and c show TEM images of Pt/CB and Pt/CA-200 obtained at 50× magnification. The Pt nanoparticles are visible as darker gray dots on the lighter carbon background.

As shown in Fig. 3a, both the Pt nanoparticles and CB powder display a considerable amount of agglomeration when CB is used as the catalyst support, while the Pt nanoparticles, shown in Fig. 3c, are much more evenly distributed and much less clustered in Pt/CA-200. The primary CB powder clumping can be explained by the strong Van der Waals stabilizing interactions due to the large surface area-to-volume ratio of CB particles. This phenomenon was also reported in other works [40]. However, for CA-200, its high mesopore volume allows for the formation of smaller particles in the step of Pt/catalyst preparation, as shown in Fig. 1b [41]. Because the particle size is smaller, the primary particles exhibit a more

Table 1
The summary of pore volume, BET surface area, and average pore diameter in CAs and CB based on NLDFT calculation.

Material	V_{total}, cm^3/g	V_{micro}, cm^3/g	V_{meso}, cm^3/g	V_{meso}, %	S_{BET}, m^2/g	S_{micro}, m^2/g	S_{meso}, m^2/g	d_{avg}, nm
CB	0.333	0.065	0.268	80.5	251	128	123	5.31
CA-100	1.292	0.211	1.081	83.7	682	471	211	7.58
CA-200	1.314	0.171	1.143	86.8	700	255	455	7.51
CA-300	1.008	0.189	0.811	81.3	626	309	317	6.44

V_{total}, total pore volume; V_{micro}, total micropore volume; V_{meso}, total mesopore volume; V_{meso}, mesopore percentage; S_{BET}, BET surface area; S_{micro}, micropore BET surface area; S_{meso}, mesopore BET surface area; d_{avg}, average pore diameter; BET, Brunauer-Emmett-Teller; CA, carbon aerogel; CB, carbon black; NLDFT, non-localized density functional theory.

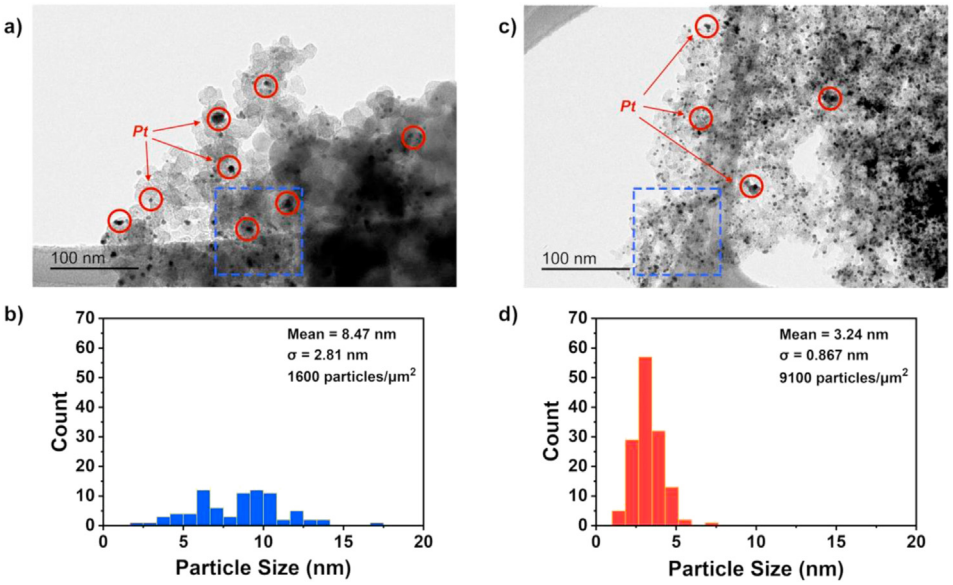

Fig. 3. (a) TEM of Pt/CB, (b) Pt particle size distribution histogram of Pt/CB, (c) TEM of CA-200, and (d) Pt particle size distribution histogram of Pt/CA-200 that were collected under the same conditions. 50× magnification was used in TEM. TEM, transmission electron microscopy; CB, carbon black.

compact packing structure, higher mechanical strength, and thus a smaller agglomerate size [42].

The Pt nanoparticle size distribution, which corresponds to TEM images, is shown in Fig. 3b and d for CB and CA-200, respectively. The mean platinum nanoparticle size was determined to be 8.47 nm and 3.24 nm in CB and in CA-200, respectively. Chen et al. [43] reported similar platinum nanoparticle size values for Pt/CB. First, it is clear to see that the average Pt nanoparticle size in CA-200 is smaller than that in CB because of the left-skewed distribution histogram. It is also noteworthy that Pt nanoparticles with diameters smaller than 2.0 nm were observed only in CA-200 but not in CB. This is because the diameter of the majority of pores in CB are <2 nm, but the average diameter of Pt nanoparticle agglomerated clusters in CB is 8.47 nm, and most of the Pt nanoparticles are blocked out of the pores of CB and accumulated on the CB exterior surface. For the Pt nanoparticles in CA-200, the large mesopores allow Pt nanoparticles to have access not only to the exterior surface area of CA-200 but also to its interior surface area of the pores. These accessible large surface areas facilitate Pt nanoparticles' uniform dispersion and less clumping on CA-200. In addition, the ECSA loss is also reported to be caused by Pt nanoparticle agglomeration [44]. From all these perspectives, CA-200 shows better properties than CB as a catalyst support in the PEMFC.

3.3. Pt/CA-200 and Pt/CB electrochemical property characterization

3.3.1. Electrochemical surface area

ECSA is a critical parameter that speaks for the intrinsic electrocatalytic activity of Pt catalysts, which is usually calculated by integration charges in the hydrogen adsorption region of the steady-state cyclic voltammogram in a supporting electrolyte (i.e., standard hydrogen electrode), based on a monolayer hydrogen adsorption charge of 0.21 mC/cm^2 on polycrystalline Pt. Fig. 4 shows the cyclic voltammogram of CA-200 and CB. A well-defined hydrogen adsorption/desorption characteristic was observed for the Pt catalysts on both CA-200 and CB. The current for Pt/CA-200 is universally higher than the current for Pt/CB for the full scan range from 0.1 to 0.85 V, except at the very low scan range (e.g., 0.1–0.11 V). The ECSA for Pt/CA-200 and Pt/CB is determined

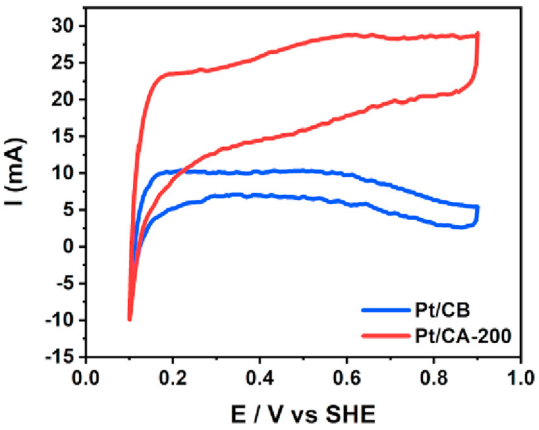

Fig. 4. Cyclic voltammogram of Pt/CB and Pt/CA-200 catalyst layer for ECSA analysis by hydrogen adsorption/desorption. Conditions: scan rate, 20 mV/s; cell, 35 °C; RH, 100% for both the anode and cathode; pressure, 1 atm. CB, carbon black; ECSA, electrochemical surface area; RH, relative humidity.

to be 188 m^2/g and 86.4 m^2/g, respectively. The data are summarized in Table 2. The observation and ECSA data agree with Pt/CA-200 and Pt/CB characterization by TEM and can be ascribed to higher Pt utilization because of the much smaller Pt nanoparticle size, uniform Pt nanoparticle distribution on the larger surface area of CA-200, better gas molecule diffusion and thus high H_2 uptake implied by CA-200 isotherms, and improved penetration of Nafion ionomer molecules, which are able to maintain a better contact of

Table 2
Pt/CB and Pt/CA-200 ECSA and ECSA ratio after various AST cycles.

AST cycles	ECSA, m^2/g		
	Pt/CB	Pt/CA-200	(Pt/CA-200)/(Pt/CB)
Initial	86.35	187.9	2.176
5000	71.36	164.8	2.309
10,000	60.16	140.3	2.332

AST, accelerated stress test; ECSA, electrochemical surface area; CB, carbon black.

Pt nanoparticles on CA and increases the overall electroconductivity of the catalyst support [45].

3.3.2. Pt/CA-200 and Pt/CB durability

To date, durability is a major barrier for PEMFC commercialization in practical stationary or transportation power generation. The durability is influenced by many interior and exterior factors, such as fuel cell design and assembly, degradation of materials, and operational conditions [46]. Although degradation is inevitable, the degradation rate can be minimized by developing better electrode materials for the PEMFC. Pt catalyst degradation is a major concern for the deterioration of the catalytic activity of Pt/catalyst support [47]. In particular, the ECSA of a platinum catalyst is reduced owing to the aggregation and dissolution of Pt nanoparticles or the detachment of platinum during the operation of the fuel cell, and thus, the oxygen reduction reaction rate of the cathode is reduced, causing a reduction in PEMFC performance. A better catalyst support is highly desired for PEMFC performance and commercialization to reduce socioeconomic issues such as climate change, air pollution, and health concerns caused by traditional fossil energy resources.

To compare the durability of the Pt/CB and Pt/CA-200 electrodes, we followed the standard DOE2020 AST cycling protocol. The MEAs were subjected to tests consisting of a total of 10,000 AST cycles, which is equivalent to 500 h of fuel cell vehicle operation, to simulate strenuous operating conditions and to induce carbon oxidation, which leads to electrode degradation and breakdown of the electrode structure [48,49]. The CV curves of the initial (e.g., 0) test and after 5,000, and 10,000 cycles of tests are illustrated in Fig. 5a and b for the Pt/CB and Pt/CA-200 MEAs, respectively. The corresponding ECSA values are tabulated in Table 2. CV curves exhibit that Pt/CA-200 MEAs globally have much higher current than Pt/CB MEAs in the course of AST testing. Even after 10,000 cycles, Pt/CA-200 still maintained higher current than initial Pt/CB MEA under the same scan conditions. As shown in Table 2, ECSA of Pt/CA-200 MEA is generally 2.2−2.3 times higher before and after AST cycling. The degradation rate (e.g., the slope of the curves in Fig. 5c) of Pt/CB is 1.8 times that of Pt/CA-200. After 10,000 cycles, Pt/CA-200 still maintained 140.3 m^2/g of ECSA, which is 1.6 times the highest ECSA of Pt/CB at its initial state. Padgett et al. [48] reported similar ECSA values and relative degradation for Pt/CB after AST cycling. This again proves the good quality control of the experiments in this study and validates the superior performance of Pt/CA-200.

Fig. 5d presents the current density retention (averaged 5 tests) after 10,000 cycles of ASTs for both Pt/CA-200 MEA and Pt/CB MEA. As shown in the figure, the Pt/CB MEA lost ~30% of current density, which is far inferior to the Pt/CA-200 MEA, which still maintains 85% of current density. In summary, as per the ECSA and current density degradation performance, the Pt/CA-200 MEA displays at least 2 times better durability, indicating that CA-200 is a superior catalyst support for PEMFCs.

The plausible structural explanation of this result is that microporous CB is heavily susceptible to catalyst coarsening by coalescence, which is due to agglomeration and pore accessibility blockage [48]. The highly mesoporous CA-200 constricts the particles within their pore structure, mitigating their coalescence. In addition, the porous mechanical structure of CA-200 exhibits a better distribution of particles in the support, which has been shown to decrease the probability of particle migration and coalescence [48]. Some advantages of the Pt/CA-200 MEA that contribute to its superior durability are less ECSA loss, larger S_{BET} to slow down the catalyst degradation, large active ECSA for chemical reactions, better catalyst and ionomer penetration into the mesopores for highly efficient catalyst utilization, and electronic conductivity.

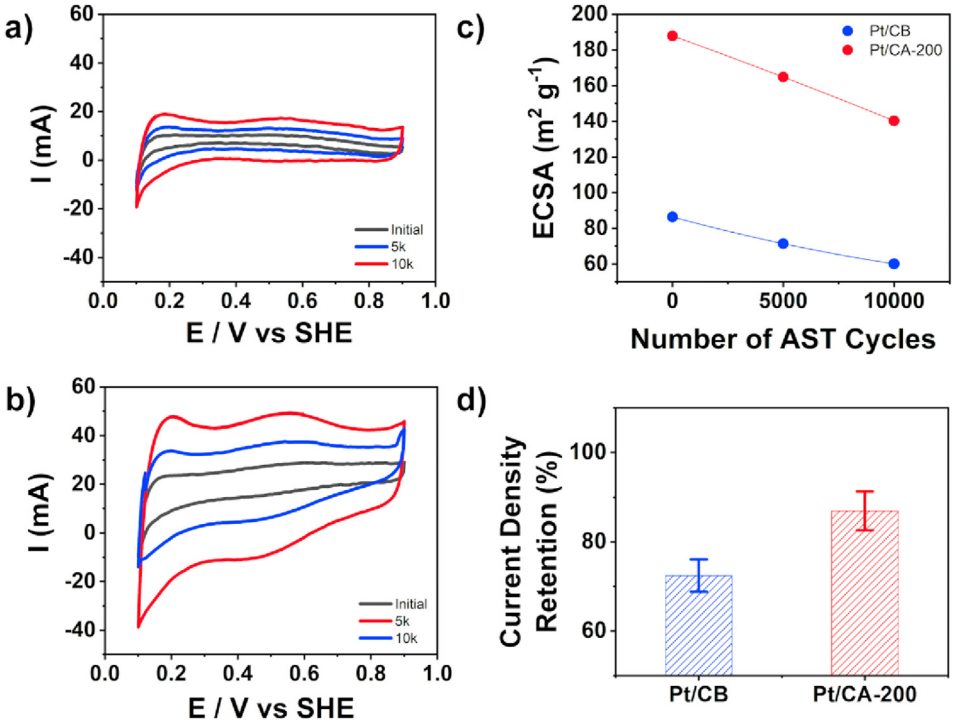

Fig. 5. Cyclic voltammetry at a 20 mV/s scan rate after the initial cycle and after 5000 and 10,000 AST cycles for (a) Pt/CB and (b) Pt/CA MEAs at 80 °C under H_2/N_2 environment, (c) ECSA degradation of Pt/CB and Pt/CA-200, and (d) current density retention percentage for Pt/CB and Pt/CA-200 after 10k AST cycles. CB, carbon black; MEA, membrane electrode assembly; CA, carbon aerogel; AST, accelerated stress test; ECSA, electrochemical surface area.

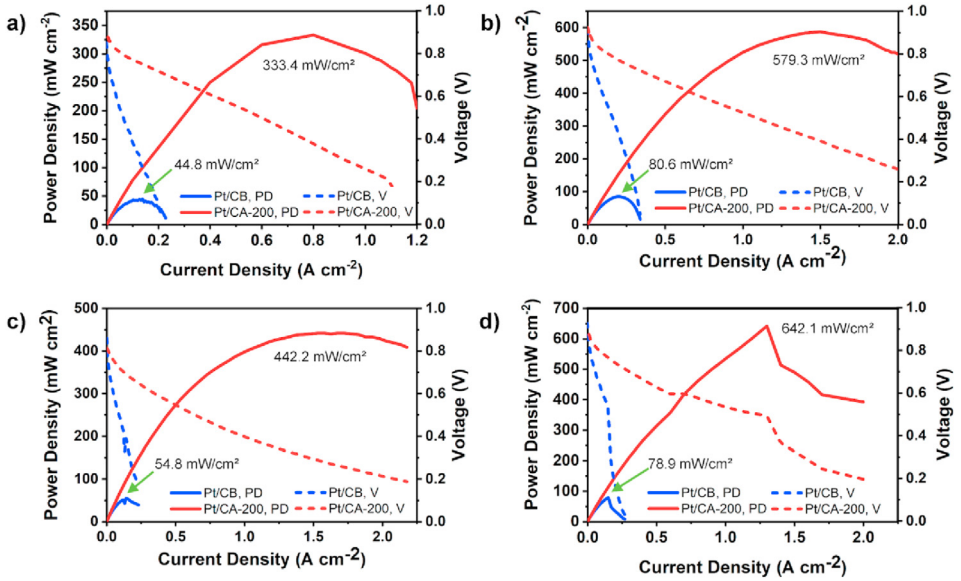

Fig. 6. Fuel cell performance at a) 60 °C under H_2/air, b) 60 °C under H_2/O_2, c) 80 °C under H_2/air, and d) 80 °C under H_2/O_2 environment. CB, carbon black.

Table 3
Comparison of peak power density and current density at 0.6 V of Pt/CB and Pt/CA-200.

Material	Power density, mW/cm^2				Current density, mA/cm^2			
	60_{Air}	60_{Oxy}	80_{Air}	80_{Oxy}	60_{Air}	60_{Oxy}	80_{Air}	80_{Oxy}
Pt/CB	44.8	80.6	54.8	78.9	3.58	9.98	4.98	10.9
Pt/CA	333.4	579.3	442.2	642.1	45.0	69.9	32.7	69.9
Percentage of increase	644%	617%	707%	713%	1157%	600%	558%	541%

CB, carbon black; CA, carbon aerogel.

3.3.3. Fuel cell test

To simulate fuel cell performance in real-world applications, both Pt/CA-200 and CB MEAs were tested under atmospheric and oxygen conditions to mimic fuel cells in cars and power plants, respectively. The polarization and power curves of Pt/CB and Pt/CA-200 electrodes under testing environments of 60 °C in H_2/air, 60 °C in H_2/O_2, 80 °C in H_2/air, and 80 °C in H_2/O_2 are shown in Fig. 6a–d, respectively. The peak power densities of the polarization curves are presented in Table 3. In addition, current densities at 0.6 V obtained from the graphs are also shown in Table 3. In Fig. 6a, we can observe that the maximum power density of the cell, P_{max} = 333.4 mW/cm^2, was recorded for Pt/CA-200 at 60 °C under H_2/air environment. This result shows a performance increase of 644% compared with the peak power density of Pt/CB, P_{max} = 44.8 mW/cm^2. Similar increases in P_{max} were observed at 60 °C under H_2/O_2, 80 °C under H_2/air, and 80 °C under H_2/O_2 environments, with an increase of 617%, 707%, and 713%, respectively. The current density of Pt/CA-200 at 0.6 V is 1157% larger or 45 mA/cm^2 and 3.58 mA/cm^2 for Pt/CA-200 and Pt/CB at 60 °C under H_2/air environment, respectively. Again, there is a similar trend of current density at 0.6 V improvements at 60 °C under H_2/O_2, 80 °C under H_2/air, and 80 °C under H_2/O_2 conditions, with increases of 600%, 557%, and 541%, respectively. It is clear that the high peak power density and high current density of Pt/CA-200 indicates its overall superior fuel cell performance.

This higher fuel cell performance from Pt/CA-200 with increasing support porosity is consistent with prior results and further demonstrates the detrimental effect of catalyst coalescence and low ECSA, which can be limited on largely mesoporous supports with catalyst surfaces that are embedded within, such as CA-200 [50,51]. The larger ECSA and higher Pt utilization, both of which are closely related to the smaller Pt nanoparticles and more uniform particle dispersion on the CA-200, were consistently observed in this study.

4. Conclusion

We have demonstrated a facile synthesis of CA and its application in the PEMFC. Its porosity was tuned, and an optimal CA, CA-200, carries a surface area of 700 m^2/g and a mesopore volume of 1.14 cm^3/g. The Pt/CA-200 was comprehensively characterized to investigate its porosity and electrochemical properties when used as a catalyst in the PEMFC under different conditions.

TEM shows Pt/CA-200 facilitates smaller Pt nanoparticle generation and better distribution. The mesopore volume of Pt/CA-200 increases 2.7 times the BET surface area and 2.2 times the ECSA compared with the conventional CB. The mesopore volume of Pt/CA-200 also increases the pore accessibility to the nanosized catalyst, Nafion® ionomer molecules, and gas molecules and thus significantly improves overall PEMFC performance by 5–7 times depending on the conditions. Standard AST testing also shows Pt/CA-200 up to two times more durable than CB.

The findings of this study show that CA is a promising candidate for the catalyst support, especially CA-200, which is comprehensively characterized and compared with conventional CB, demonstrates its notable advancements to the PEMFC. With superior fuel cell performance, CA-200 can make clean PEMFC technology more accessible to the general public. Ultimately, replacing gasoline with CA-200–equipped fuel cells will help reduce the range of air pollutant emission, which not only mitigates the current climate

change crisis but also diminishes public health challenges caused by poor air quality and climate change. Future work will focus on improving Pt deposition technology, optimizing ionomer loading, and investigating microscale gas molecule transportation between phases to further enhance the design and collective performance of the CA-200 PEMFC.

Credit author statement

Kevin Gu: Conceptualization, Methodology, Formal analysis, Investigation, Data Curation, Writing - Original Draft, Writing - Review & Editing, Visualization. **Eric J. Kim:** Conceptualization, Methodology, Formal analysis, Investigation, Data Curation, Writing - Original Draft, Writing - Review & Editing, Visualization. **Sunil K. Sharma:** Validation, Investigation, Data Curation. **Priyanka R. Sharma:** Validation. **Stoyan Bliznakov:** Validation, Investigation. **Benjamin S. Hsiao:** Resources. **Miriam H. Rafailovich:** Investigation, Resources, Supervision, Funding acquisition.

Data availability

The raw/processed data required to reproduce these findings cannot be shared at this time as the data also form part of an ongoing study.

Declaration of Competing Interest

The authors declare that they have no known competing financial interests or personal relationships that could have appeared to influence the work reported in this paper.

Acknowledgments

The authors express their appreciation to the Garcia Center for Polymers at Engineered Interfaces and Center for Integrated Electric Energy Systems for their support and access to their facilities. This work was supported by the Louis Morin Charitable Trust.

Appendix A. Supplementary data

Supplementary data to this article can be found online at https://doi.org/10.1016/j.mtener.2020.100560.

References

[1] O. Edenhofer, R. Pichs-Madruga, Y. Sokona, J.C. Minx, E. Farahani, S. Kadner, K. Seyboth, A. Adler, I. Baum, S. Brunner, P. Eickemeier, B. Kriemann, J. Savolainen, S. Schlömer, C. von Stechow, T. Zwickel, Climate Change 2014 Mitigation of Climate Change, (n.d.), https://www.ipcc.ch/report/ar5/wg3/.

[2] M. Krzyżanowski, B. Kuna-Dibbert, J. Schneider, Health Effects of Transport-Related Air Pollution, WHO Regional Office Europe, 2005. https://www.euro.who.int/en/publications/abstracts/health-effects-of-transport-related-air-pollution.

[3] J.O. Anderson, J.G. Thundiyil, A. Stolbach, Clearing the Air: A Review of the Effects of Particulate Matter Air Pollution on Human Health, J. Med. Toxicol. (2012), https://doi.org/10.1007/s13181-011-0203-1.

[4] C. Abbey, G. Joos, Supercapacitor energy storage for wind energy applications, IEEE Trans. Ind. Appl. 43 (2007) 769–776, https://doi.org/10.1109/tia.2007.895768.

[5] G. Gorgolis, D. Karamanis, Solar energy materials for glazing technologies, Sol. Energy Mater. Sol. Cells 144 (2016) 559–578, https://doi.org/10.1016/j.solmat.2015.09.040.

[6] S.J. Peighambardoust, S. Rowshanzamira, M. Amjadia, Review of the proton exchange membranes for fuel cell applications, Int. J. Hydrogen Energy 35 (2010) 9349–9384, https://doi.org/10.1016/j.ijhydene.2010.05.017.

[7] W. Lubitz, W. Tumas, Hydrogen: an overview, Chem. Rev. (2007), https://doi.org/10.1021/cr050200z.

[8] I. Staffell, D. Scamman, A.V. Abad, P. Balcombe, P.E. Dodds, P. Ekins, N. Shah, K.R. Ward, The role of hydrogen and fuel cells in the global energy system, Energy Environ. Sci. 12 (2019) 463–491, https://doi.org/10.1039/C8EE01157E.

[9] V.R. Stamenkovic, B. Fowler, B.S. Mun, G. Wang, P.N. Ross, C.A. Lucas, N.M. Marković, Improved oxygen reduction activity on Pt3Ni(111) via increased surface site availability, Science 315 (2007) 493–497, https://doi.org/10.1126/science.1135941.

[10] Y. Yu, H. Li, H. Wang, X.-Z. Yuan, G. Wang, M. Pan, A review on performance degradation of proton exchange membrane fuel cells during startup and shutdown processes: causes, consequences, and mitigation strategies, J. Power Sources 205 (2012) 10–23, https://doi.org/10.1016/j.jpowsour.2012.01.059.

[11] J. Marquis, M.O. Coppens, Achieving ultra-high platinum utilization via optimization of PEM fuel cell cathode catalyst layer microstructure, Chem. Eng. Sci. 102 (2013) 151–162, https://doi.org/10.1016/j.ces.2013.08.003.

[12] Y. Show, Y. Ueno, Formation of platinum catalyst on carbon black using an in-liquid plasma method for fuel cells, Nanomaterials 7 (2017) 31, https://doi.org/10.1039/C4TA02952F.

[13] Achievement of distinctively high durability at nanosized Pt catalysts supported on carbon black for fuel cell cathodes, J. Electroanal. Chem. 819 (2018) 359–364, https://doi.org/10.1016/j.jelechem.2017.11.017.

[14] J.S. Lee, G.S. Park, S.T. Kim, M. Liu, J. Cho, A highly efficient electrocatalyst for the oxygen reduction reaction: N-doped ketjenblack incorporated into Fe/Fe3C-functionalized melamine foam, Angew. Chem., Int. Ed. Engl. 52 (2013) 1026–1030, https://doi.org/10.1002/anie.201207193.

[15] A. Roy, M.R. Talarposhti, S.J. Normile, I.V. Zenyuk, V. De Andrade, K. Artyushkova, A. Serov, P. Atanassov, Nickel–copper supported on a carbon black hydrogen oxidation catalyst integrated into an anion-exchange membrane fuel cell, Sustainable Energy Fuels 2 (2018) 2268–2275.

[16] C. Wang, M. Waje, X. Wang, J.M. Tang, R.C. Haddon, Yan, Proton Exchange Membrane Fuel Cells with Carbon Nanotube Based Electrodes, Nano Lett. (2004), https://doi.org/10.1021/nl034952p.

[17] B.P. Vinayan, R. Imran Jafri, R. Nagar, N. Rajalakshmi, K. Sethupathi, S. Ramaprabhu, Catalytic activity of platinum–cobalt alloy nanoparticles decorated functionalized multiwalled carbon nanotubes for oxygen reduction reaction in PEMFC, Int. J. Hydrogen Energy 37 (2012) 412–421, https://doi.org/10.1016/j.ijhydene.2011.09.069.

[18] M.N. Banis, S. Sun, X. Meng, Y. Zhang, Z. Wang, R. Li, M. Cai, T.-K. Sham, X. Sun, $TiSi_2O_x$ coated N-doped carbon nanotubes as Pt catalyst support for the oxygen reduction reaction in PEMFCs, J. Phys. Chem. C 117 (2013) 15457–15467, https://doi.org/10.1021/jp3118874.

[19] Z.D. Wei, C. Yan, Y. Tan, L. Li, C.X. Sun, Z.G. Shao, P.K. Shen, H.W. Dong, Spontaneous reduction of Pt(IV) onto the sidewalls of functionalized multi-walled carbon nanotubes as catalysts for oxygen reduction reaction in PEMFCs, J. Phys. Chem. C 112 (2008) 2671–2677, https://doi.org/10.1021/jp709936p.

[20] M.R. Berber, I.H. Hafez, T. Fujigaya, N. Nakashima, A highly durable fuel cell electrocatalyst based on double-polymer-coated carbon nanotubes, Sci. Rep. 5 (2015) 1–11, https://doi.org/10.1038/srep16711.

[21] Y. Devrim, A. Albostan, Graphene-supported platinum catalyst-based membrane electrode assembly for PEM fuel cell, J. Electron. Mater. 45 (2016) 3900–3907, https://doi.org/10.1007/s11664-016-4703-2.

[22] S. Stambula, N. Gauquelin, M. Bugnet, S. Gorantla, S. Turner, S. Sun, J. Liu, G. Zhang, X. Sun, G.A. Botton, Chemical structure of nitrogen-doped graphene with single platinum atoms and atomic clusters as a platform for the PEMFC electrode, J. Phys. Chem. C 118 (2014) 3890–3900, https://doi.org/10.1021/jp408979h.

[23] A. Marinoiu, C. Teodorescu, E. Carcadea, M. Raceanu, M. Varlam, C. Cobzaru, I. Stefanescu, Graphene-based materials used as the catalyst support for PEMFC applications, Mater. Today: Proc. 2 (2015) 3797–3805, https://doi.org/10.1016/j.matpr.2015.08.013.

[24] J. Liu, D. Takeshi, K. Sasaki, S.M. Lyth, Defective graphene foam: a platinum catalyst support for PEMFCs, J. Electrochem. Soc. 161 (2014) F838–F844, https://doi.org/10.1149/2.0231409jes.

[25] M.B. Sassinn, Y. Garsany, R.W. Atkinson III, R.M.E. Hjelm, K.E. Swider-Lyons, Understanding the interplay between cathode catalyst layer porosity and thickness on transport limitations en route to high-performance PEMFCs, Int. J. Hydrogen Energy 44 (2019) 16944–16955, https://doi.org/10.1016/j.ijhydene.2019.04.194.

[26] S. Samad, K.S. Loh, W.Y. Wong, T.K. Lee, J. Sunarso, S.T. Chong, W.R.W. Daud, Carbon and non-carbon support materials for platinum-based catalysts in fuel cells, Int. J. Hydrogen Energy 43 (2018) 7823–7854, https://doi.org/10.1016/j.ijhydene.2018.02.154.

[27] C. Luo, H. Xie, Q. Wang, G. Luo, C. Liu, A review of the application and performance of carbon nanotubes in fuel cells, J. Nanomater. 2015 (2015), https://doi.org/10.1155/2015/560392.

[28] A.Z. Weber, A. Kusoglu, Unexplained transport resistances for low-loaded fuel-cell catalyst layers, J. Mater. Chem. A Mater. Energy Sustain. 2 (2014) 17207–17211, https://doi.org/10.1039/C4TA02952F.

[29] X. Zhao, W. Li, Y. Fu, A. Manthiram, Influence of ionomer content on the proton conduction and oxygen transport in the carbon-supported catalyst layers in DMFC, Int. J. Hydrogen Energy 37 (2012) 9845–9852, https://doi.org/10.1016/j.ijhydene.2012.03.107.

[30] N. Nonoyama, S. Okazaki, A.Z. Weber, Y. Ikogi, T. Yoshida, Analysis of oxygen-transport diffusion resistance in proton-exchange-membrane fuel cells, J. Electrochem. Soc. 158 (2011) B416, https://doi.org/10.1149/1.3546038.

[31] S. Cruz-Manzo, R. Chen, Electrochemical impedance study on estimating the mass transport resistance in the polymer electrolyte fuel cell cathode catalyst

layer, J. Electroanal. Chem. 702 (2013) 45–48, https://doi.org/10.1016/j.jelechem.2013.05.008.
[32] A. Kongkanand, M.F. Mathias, The priority and challenge of high-power performance of low-platinum proton-exchange membrane fuel cells, J. Phys. Chem. Lett. 7 (2016) 1127–1137, https://doi.org/10.1021/acs.jpclett.6b00216.
[33] V. Yarlagadda, M.K. Carpenter, T.E. Moylan, R.S. Kukreja, R. Koestner, W. Gu, L. Thompson, A. Kongkanand, Boosting fuel cell performance with accessible carbon mesopores, ACS Energy Lett. 3 (2018) 618–621, https://doi.org/10.1021/acsenergylett.8b00186.
[34] S. Kumaraguru, Durable High-Power Membrane Electrode Assemblies with Low Platinum Loading, 2018. https://www.hydrogen.energy.gov/pdfs/progress18/fc_kumaraguru_2018.pdf.
[35] J.B. Xu, T.S. Zhao, Mesoporous carbon with uniquely combined electrochemical and mass transport characteristics for polymer electrolyte membrane fuel cells, RSC Adv. 3 (2012) 16–24, https://doi.org/10.1039/C2RA22279E.
[36] J. Feng, J. Feng, C. Zhang, Shrinkage and Pore Structure in Preparation of Carbon Aerogels, 2011, https://doi.org/10.1007/s10971-011-2514-8.
[37] P. Kim, J.B. Joo, W. Kim, J. Kim, I.K. Song, J. Yi, NaBH4-assisted ethylene glycol reduction for preparation of carbon-supported Pt catalyst for methanol electro-oxidation, J. Power Sources 160 (2006) 987–990, https://doi.org/10.1016/j.jpowsour.2006.02.050.
[38] IUPAC, Reporting Physisorption Data for Gas/Solid Systems with Special Reference to the Determination of Surface Area and Porosity, 1984. http://publications.iupac.org/pac/pdf/1985/pdf/5704x0603.pdf. (Accessed 1 July 2020).
[39] T. Soboleva, X. Zhao, K. Malek, Z. Xie, T. Navessin, S. Holdcroft, On the micro-, meso-, and macroporous structures of polymer electrolyte membrane fuel cell catalyst layers, ACS Appl. Mater. Interfaces 2 (2010) 375–384, https://doi.org/10.1021/am900600y.
[40] J. Marie, S. Berthon-Fabry, M. Chatenet, E. Chainet, R. Pirard, N. Cornet, P. Achard, Platinum supported on resorcinol–formaldehyde based carbon aerogels for PEMFC electrodes: influence of the carbon support on electrocatalytic properties, J. Appl. Electrochem. 37 (2006) 147–153, https://doi.org/10.1007/s10800-006-9226-8.
[41] A. Fabre, S. Salameh, L.C. Ciacchi, M.T. Kreutzer, J.R. van Ommen, Contact mechanics of highly porous oxide nanoparticle agglomerates, J. Nanoparticle Res. 18 (2016) 200, https://doi.org/10.1007/s11051-016-3500-4.
[42] X. Deng, Z. Huang, W. Wang, R.N. Davé, Investigation of nanoparticle agglomerates properties using Monte Carlo simulations, Adv. Powder Technol. 27 (2016) 1971–1979, https://doi.org/10.1016/j.apt.2016.06.029.
[43] G. Chen, D.A. Delafuente, S. Sarangapani, T.E. Mallouk, Combinatorial discovery of bifunctional oxygen reduction — water oxidation electrocatalysts for regenerative fuel cells, Catal. Today 67 (2001) 341–355, https://doi.org/10.1016/S0920-5861(01)00327-3.
[44] N. Dyantyi, A. Parsons, P. Bujlo, S. Pasupathi, Behavioural study of PEMFC during start-up/shutdown cycling for aeronautic applications, Mater. Renewable Sustain. Energy 8 (2019) 1–8, https://doi.org/10.1007/s40243-019-0141-4.
[45] S.J. Lee, S. Mukerjee, T.-H. Lee, Effects of Nafion impregnation on performances of PEMFC electrodes, Electrochim. Acta 43 (1998) 3693–3701, https://doi.org/10.1016/S0013-4686(98)00127-3.
[46] J. Wu, X.Z. Yuan, J.J. Martin, H. Wang, J. Zhang, J. Shen, S. Wu, W. Merida, A review of PEM fuel cell durability: degradation mechanisms and mitigation strategies, J. Power Sources 184 (2008) 104–119, https://doi.org/10.1016/j.jpowsour.2008.06.006.
[47] S. Yang, S. Choi, Y. Kim, J. Yoon, S. Im, H. Choo, Improvement of fuel cell durability performance by avoiding high voltage, Int. J. Automot. Technol. 20 (2019) 1113–1121, https://doi.org/10.1007/s12239-019-0104-x.
[48] E. Padgett, V. Yarlagadda, M.E. Holtz, M. Ko, B.D.A. Levin, R.S. Kukreja, J.M. Ziegelbauer, R.N. Andrews, J. Ilavsky, A. Kongkanand, D.A. Muller, Mitigation of PEM fuel cell catalyst degradation with porous carbon supports, J. Electrochem. Soc. 166 (2019) F198, https://doi.org/10.1016/j.ijhydene.2008.10.012.
[49] S. Zhang, X. Yuan, HaijiangWang, W. Mérida, H. Zhu, J. Shen, S. Wu, J. Zhang, A review of accelerated stress tests of MEA durability in PEM fuel cells, Int. J. Hydrogen Energy 34 (2009) 388–404, https://doi.org/10.1016/j.ijhydene.2008.10.012.
[50] E. Padgett, N. Andrejevic, Z. Liu, A. Kongkanand, W. Gu, Koji Moriyama, Y. Jiang, S. Kumaraguru, T.E. Moylan, R. Kukreja, D.A. Muller, Connecting fuel cell catalyst nanostructure and accessibility using quantitative cryo-STEM tomography, J. Electrochem. Soc. (2018), https://doi.org/10.1149/2.0541803jes.
[51] R. Subbaraman, D. Strmcnik, A.P. Paulikas, V.R. Stamenkovic, N.M. Markovic, Oxygen reduction reaction at three-phase interfaces, ChemPhysChem 11 (2010) 2825–2833, https://doi.org/10.1002/cphc.201000190.